UCLA
UCLA Previously Published Works

Title

Atomic Environments in N-Containing Graphitic Carbon Probed by First-Principles Calculations and Solid-State Nuclear Magnetic Resonance

Permalink

https://escholarship.org/uc/item/6371j35m

Journal

The Journal of Physical Chemistry C, 125(16)

ISSN

1932-7447

Authors

Wei, Ziyang
Becwar, Shona M
Chmelka, Bradley F
et al.

Publication Date

2021-04-29

DOI

10.1021/acs.jpcc.1c00511

Supplemental Material

https://escholarship.org/uc/item/6371j35m#supplemental

Peer reviewed

eScholarship.org Powered by the California Digital Library
University of California

Atomic Environments in N-containing Graphitic Carbon Probed by First-principle Calculations and Solid-State Nuclear Magnetic Resonance

Ziyang Wei,[†] Shona M. Becwar,[‡] Bradley F. Chmelka,[‡] and Philippe Sautet[*,†,¶]

†*Department of Chemistry and Biochemistry, University of California, Los Angeles, California, 90095, U.S.A.*

‡*Department of Chemical Engineering, University of California, Santa Barbara, California, 93106, U.S.A.*

¶*Department of Chemical and Biomolecular Engineering, University of California, Los Angeles, California, 90095, U.S.A.*

E-mail: sautet@ucla.edu

Abstract

In order to understand the nature and structure of N doping centers in carbon materials, we combine 2D solid-state NMR experiments and chemical shift calculations for N, C, H nuclei from density functional theory (DFT). Comparisons of predicted chemical shifts with experimental 2D ^{13}C-^{15}N spectra show good agreement and the calculations explain the spectral broadening seen in the experiments. The major differences between the chemical shifts of graphitic/pyridinic/pyrrolic N-moieties are understood by comparing the electronegativities of the various environments. Moreover, the signal broadening is explained using four different factors: (1) the standalone N/C geometry, (2) the effect of a second N atom nearby, (3) the first or second neighbor C atom difference, and (4) the influence of residual water, which is important to understand the

eletrocatalytic environment. An intuitive correlation between the charge of the probed atom and the chemical shift is validated: the smaller the charge, i.e., higher electron density, the more shielded the nucleus is, and hence the smaller the associated chemical shift. These results can improve the understanding of the nature of hetreoatom sites in nitrogen-carbon materials and contribute to the rational design of these materials with desired electronic properties and improved electrochemical performance.

Introduction

Nitrogen-doped graphenes have emerged as an important class of materials due to their attractive electronic properties with applications as electrodes,[1,2] electrocatalysts[3,4] and catalyst supports.[5] Typical N doping of graphene, however, provides a mix of different local N structures where the simplest species[6] are pyrrolic, pyridinic, and graphitic nitrogen. Materials with high extents of doping are desired, and present a large range of lateral assembly and interactions among these three basic types of N centers. In order to establish tentative perfomance-structure relations, numerous efforts have been made to detect the local environments of N-doped graphene via tools including Raman spectroscopy,[7] X-ray photoelectron spectroscopy[1,8] (XPS), scanning tunneling microscopy[7,9] (STM), and nuclear magnetic resonance[10] (NMR) spectroscopy. However, Raman spectroscopy can provide only limited insights into the detailed local structure of N atoms since distributions of various local moieties are present, which limit the resolution. XPS, in principle, is sensitive to the local bonding near surfaces, but the slight differences in binding energies are hard to accurately simulate and interpret, especially since the resolution is low.[1,8] STM provides high resolution images of local structures, but the sampling of the various sites is challenging. Two-dimensional (2D) solid-state NMR (ssNMR), benefitting from advances in sensitivity and resolution in the recent years,[11] is a promising tool to cast light onto the atomic-scale structure of these materials and is particularly amenable to combined analyses with first-principles calculations.

Although solid-state NMR has been utilized to determine the local structures of different periodic carbon materials,[10,12] theoretical predictions of NMR spectral features from ab initio calculations are generally scarce, limiting the accuracy in the interpretation of the spectra in terms of local structures. Such predictions had been limited to finite systems until Mauri et al. extended the theory to periodic systems.[13] Mauri et al. later made improvements to account for the translational invariance when the projector augmented wave (PAW) method is used; this is known as the gauge including projector augmented wave (GIPAW) approach.[14,15] The GIPAW method has been utilized in various systems to represent the influences of structural variations on NMR signals.[16–19]

Periodic models are important to representing the variations in NMR chemical shifts, especially for systems with delocalized wavefunctions. Thonhauser et al. investigated both finite and periodic carbon systems and showed that a relatively large finite system, coronene, is still different from a periodic model.[20] Results of Özcan et al.[21] also showed in the case of graphene that for cluster models, five to six concentric hexagonal shells, i.e., 150 to 216 C atoms in the model, are needed to achieve a converged ^{13}C chemical shifts on center C atoms at the level of 5 ppm, in line with the results of Vähäkangas et al.[22] The results of Skachkov et al.[23] and de Souza et al.[24] are achieved using periodic graphene models, although the reported ^{13}C chemical shifts are different from the value reported by Thonhasuer (roughly by 10 ppm). Instead, results of Skachkov et al.[23] and de Souza et al.[24] match better with the value obtained by Casabianca[25] using a cluster model. Moreover, none of these studies investigated the effect of N-heteroatoms. For the N-doped graphene system, to the best of our knowledge, the only relevant work has been done by Zhang et al. using cluster models[26] and there is no study done using periodic models.

In this work, density functional theory (DFT)-based first-principles calculations are performed on periodic N-doped graphene models to simulate a 2D ^{13}C-^{15}N heteronuclear multiple quantum coherence (HMQC) spectrum, in order to understand the relation between local structure and ^{13}C or ^{15}N chemical shifts. Results are compared to a experimental 2D

NMR spectra and allow a more detailed interpretation of it. Various local structures with a mix of multiple basic N species are modeled to provide insights into the structure-related broadening, which can be further decomposed into (1) standalone geometry effects, and (2) influences of additional proximate N atoms. The influence of a small amount of adsorbed water is modeled by adding explicitly water molecules to reflect the experimental measurement condition. In order to better understand the link between local structure and chemical shift, the relationships between local structure, atomic charge and chemical shifts are discussed, enabling a more detailed understanding of the influence of N doping motifs on the electronic structure. These results open the rational design of N-doped carbon materials with desired electronic properties to improve electrochemical performance.

Methods

The Vienna Ab initio Simulation Package[27] (VASP) was used for calculations. The Perdew–Burke-Ernzerhof[28] (PBE) exchange correlation functional at the generalized gradient approximation (GGA) level is used. The density-dependent dispersion correction (dDsC)[29,30] Van der Waals correction was applied for all structures. Three different sets of graphene structures were used: a hexagonal terrace model which consists of 72 C atoms (6×6 supercell), an armchair edge model which consists of 66 C atoms and 12 H atoms (before substitution with N), and a zigzag edge model consisting of 40 C atoms and 8 H atoms. The vacuum in the z-axis was set to 20Å. For the armchair/zigzag ribbon model, the in plane vacuum between the ribbons was at least 15Å. For geometry optimizations, a Monkhorst-Pack 3×3×1 k-point mesh was used for terrace model, 1×3×1 for armchair and 3×1×1 for zigzag. For NMR calculation, a 5×5×1 k-point mesh was used for terrace model, 1×7×1 for armchair and 7×1×1 for zigzag. The test for the convergence of the chemical shifts in non-doped models with respect to the k-points mesh is shown in SI table S1, and convergence to the level of 1-2 ppm was achieved.

All the calculations were developed on a basis set of plane waves. A gaussian smearing with sigma value of 0.1 eV was used through all calculations. For energy calculations, a cutoff energy for the plane wave basis set at 500 eV and an electronic step convergence criterion of 10^{-6} eV were used. For geometry optimizations, forces were optimized to 0.02 eV/Å. For NMR calculations, a cutoff energy for the plane wave basis set at 600 eV and an electronic step convergence criterion of 10^{-10} eV were set for most cases due to the requirement of such calculations. For some models (a full list can be found in SI section 2) that do not converge under this criterion, electronic step convergence criterion may be loosened to at most 10^{-7} eV and it has been tested on the graphitic N system that the influence on the calculated NMR chemical shifts is only up to 0.01 ppm, as shown in SI Fig. S1. The variation of the chemical shifts of non-doped models with respect to the cutoff energy is shown in SI table S2, and convergence to the level of 1 ppm was achieved for a value of 600 eV. The accurate precision setting was always used. Default values are used for the order of the stencils used to calculate the magnetic susceptibility and the step size for the finite difference k-space derivative, corresponding to equations 38, 40, and 47 in the work of Yates et al.[15]

VASP outputs the chemical shift tensor following the convention $\delta_{11} > \delta_{22} > \delta_{33}$ and the isotropic shift is calculated as:[31]

$$\delta_{iso} = \frac{\delta_{11} + \delta_{22} + \delta_{33}}{3} \tag{1}$$

The output values without core contribution were used as this will only lead to negligible difference of smaller than 0.001 ppm, as shown in SI table S3. We used the values without the **G=0** contribution since the **G=0** contribution is not a bulk property and is affected by the surface currents that appear on the surface of the sample.[14] VASP assumes a spherical shape for the **G=0** contribution,[14] which may not be the case for the N-doped graphene sample. More details can be found in SI section 5. The conversion to a value that is amenable to

experimental measurement and comparison was done via:[20,23,24]

$$\delta = \delta_{system,calc} - \delta_{ref,calc} + \delta_{ref,exp} \tag{2}$$

The reference system here is chosen as α glycine for ^{13}C, ^{15}N and ^{1}H. The experimental values used are 33.4 ppm for $\delta_{ref,exp,N}$, 172.7 ppm for $\delta_{ref,exp,C}$ and 3.54 ppm for $\delta_{ref,exp,H}$. It is worth mentioning that the $\delta_{ref,exp,H}$ is an average chemical shift value of three H atoms in the NH_3 group of glycine.[19] Note that the reference values for the ^{13}C, ^{15}N, and ^{1}H isotropic chemical shifts are consistent relative to commonly used standards: tetramethylsilane (TMS) as 0 ppm for ^{13}C and ^{1}H and liquid ammonia as 0 ppm[32] for ^{15}N. The CHARGEMOL package is used to calculate the Density Derived Electrostatic and Chemical (DDEC6) charge[33,34] based on VASP charge density.

For the construction of 2D ^{13}C-^{15}N spectra, we consider the first neighbor C-N pairs since the experimental dipole-mediated 2D NMR spectrum depicts signal intensity that is proportional to r^{-3}, where r is the distance between the two nuclei.[35,36] For pristine graphene, the second neighbor distance in the network is 1.73 times the first neighbor distance. This ratio is maintained after geometry optimizations in graphitic N and pyridinic N models, whereas in pyrrolic N models, the ratio is found to be 1.54. As the result, the 2D NMR signal intensity from a second neighbor will be only roughly one fifth compared to the signal strength arising from a first neighbor in graphitic or pyridinic N models, and one fourth in pyrrolic N models.

Experimentally, a mesoporous N-carbon material containing 16 atom% N was synthesized from a 1:3 molar ratio of cyclohexanehexone octahydrate and uniformly ^{13}C,^{15}N-enriched urea, with the synthesis reported by Fechler et al.[37] Nuclear enrichment made solid-state NMR characterization of the N-carbons possible. ^{13}C and ^{15}N chemical shifts were referenced to their respective values in uniformly ^{13}C,^{15}N-enriched glycine powder, using the same values as mentioned in the computational settings. The carbon materials were diluted with KBr at

a sample:KBr ratio of 1:3 w/w before being loaded into the MAS rotor. The KBr served as both an internal temperature probe[38] and to reduce undesirable sample heating that may arise from rapid rotation of conductive samples in the high magnetic field required for the NMR measurements.[39]

Solid-state two-dimensional (2D) ^{13}C-^{15}N heteronuclear multiple quantum coherence (HMQC) experiments were used to correlate ^{13}C and ^{15}N isotropic chemical shifts of ^{13}C and ^{15}N nuclei that are dipole-dipole-coupled through space. A schematic diagram of the 2D NMR pulse sequence is provided as SI Fig. S2a. Briefly, the solid-state dipolar-mediated ^{13}C-^{15}N HQMC NMR spectrum was acquired using the $SR4_1^2$ sequence to filter polarization transfer from ^{13}C to ^{15}N (for indirect detection) and back to the ^{13}C (for direct detection). These experiments were performed with 100 kHz ^{1}H decoupling, using zirconia rotors, Vespel caps, and under 8 kHz MAS on a Bruker AVANCE II HD 400 DNP-NMR spectrometer with a 9.4 T superconducting magnet operating at 400.20, 100.64, and 40.56 MHz for ^{1}H, ^{13}C, and ^{15}N nuclei, respectively, and equipped with a variable-temperature 3.2 mm HXY MAS probehead. $SR4_1^2$ was used as the dipolar recoupling scheme according to Hu et al.[40] Heteronuclear ^{13}C-^{15}N dipole-dipole couplings scale with respect to the cube of the distance separating two nuclear spins,[35,36] making these measurements sensitive principally to ^{13}C and ^{15}N nuclei that are covalently bonded directly, or to a lesser extent, by weak next-nearest neighbor interactions. The latter contribute negligibly to the overall measured signal intensity as consequence of the short ^{13}C-^{15}N recoupling times used here (0.6 ms, sensitive out to 2–3 bond distances),[41] but preferentially detect dipolar-coupled nuclei over shorter (1-2 bond) distances. The 2D dipole-mediated ^{13}C-^{15}N HMQC NMR spectrum[42] was acquired using 1024 transients, with 32 t_1 increments in the indirect dimension in STATES-TPPI acquisition mode. Recycle times of 10 s (corresponding to 1.3 T_1 of ^{15}N nuclei) were used for maximum signal sensitivity. Low-temperature conditions were used to improve NMR signal sensitivity through enhanced polarization from the Boltzmann distribution and to mitigate the influences of rapid nuclear spin relaxation effects. The temperature measured in the

MAS gas stream nearest to the stator was 95 K, and the actual sample temperature was estimated from ^{79}Br T_1 relaxation measurements to be *ca.* 99 K.

Similarly, 2D ^{15}N-^{1}H heteronuclear correlation (HETCOR)-MAS experiments were used to correlate ^{1}H and ^{15}N isotropic chemical shifts of ^{1}H and ^{15}N nuclear spin pairs that are dipole-dipole-coupled through space over sub-nanometer distances and corroborate the assignment of pyrrolic N. A schematic diagram of the 2D NMR pulse sequence is provided as SI Fig. S2b. Specifically, following a 90 degree pulse, ^{1}H polarization was allowed to evolve for incremented durations (for indirect detection), after which a shaped pulse was used to transfer ^{1}H polarization to dipole-dipole-coupled ^{15}N nuclei for direct detection. The N-doped material was exposed to atmospheric conditions for one week, and surface adsorbed water accounted for 0.5 mass% of the sample. These experiments were performed using zirconia rotors, Vespel caps, and under 10 kHz MAS on a 500 MHz Bruker AVANCE NMR spectrometer with a 11.7 T superconducting magnet operating at 500.24 and 50.69 MHz for ^{1}H and ^{15}N nuclei, respectively, and equipped with a 4 mm HXY MAS probehead. The spectrum was acquired at room temperature, with a contact time of 3000 μs, and 4000 scans.

Results and Discussion

DFT calculations are first performed on non-doped graphene systems to investigate ^{13}C chemical shifts and validate the computational parameters. The structures of the three basic models without N doping are shown in Fig. 1, and some characteristic structures with N doping are shown in Fig. 2. The numbers on the C atoms correspond to those of Table 1.

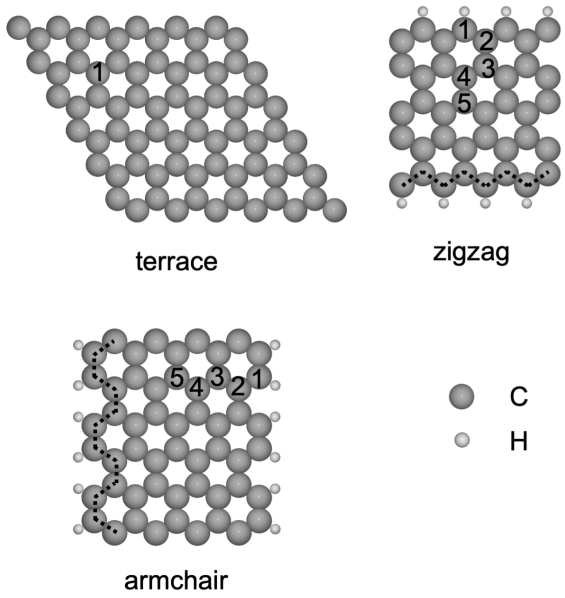

Figure 1: Atomic structures of the three basic unit cell models used in this study. The terrace model is 2D, while the armchair and the zigzag ribbons are 1D. One or two long repeat vectors are added to generate a 3D structure for the plane wave calculation. Atom numbers correspond to the values shown in Table 1, with atoms depicted as follows: grey: C, white: H. Dotted lines indicate the armchair and zigzag edges.

The graphene terrace atom is calculated to have a ^{13}C isotropic chemical shift of 119.2 ppm, which matches the experimental range between 117 and 123 ppm in the literature.[43–46] Also, compared with other computational results, our result generally matches the 118.0 ppm value reported by Thonhauser et al.,[20] but is roughly 7 ppm lower than the values reported by Skachkov et al.,[23] 127.1 ppm, and de Souza et al.,[24] 127.6 ppm. Thonhauser used Quantum Espresso with benzene as the reference molecule and Skachkov used ADF-BAND with TMS as the reference molecule. The reference difference may lead to this 7 ppm difference. However, the difference between Thonhauser and de Souza is unexplained as they both use Quantum Espresso with benzene as the reference molecule. The center C atoms in our zigzag and armchair models are calculated to have a ^{13}C chemical shift value of 108.6 ppm and 111.3 ppm, which is slightly smaller than the ^{13}C chemical shift in the terrace model by 10 and 8 ppm, respectively. Further increasing the thickness of the both models

cannot improve the match, as shown in SI table S4, and the thicknesses of both models are used through this work: 9 for armchair model and 5 for zigzag model. We have checked the influence of multilayer stacking by comparing graphene and graphite: ^{13}C isotropic chemical shift values change from 119.2 ppm to 120.3 ppm and 123.7 ppm for inequivalent sites in graphite. The values match well with experimental results[47,48] around 119 ppm and the trend matches the results of de Souza.[24] We focus on single layer models in this study since the effects will be smaller than 5 ppm.

Table 1: ^{13}C isotropic chemical shifts of different C atoms in terrace, zigzag and armchair models. Labelled atoms are shown in Fig 1.

Model	Atom	^{13}C Chemical Shift (ppm)
Terrace	1	119.2
Zigzag	1	117.0
	2	124.4
	3	111.6
	4	110.8
	5	108.6
Armchair	1	110.0
	2	116.6
	3	112.5
	4	110.2
	5	111.3

Agreement of theoretically predicted chemical shifts with experimental data for the non-doped systems validates the general modeling approach. Thus, N-doped systems are calculated with the abovementioned settings. We first investigate different structure models with one N atom: a graphitic N atom in a graphene terrace model (Fig. 2 structure 1), a pyrrolic N atom at an armchair edge (Fig. 2 structure 4) and a pyridinic N atom at a zigzag edge (Fig. 2 structure 2) and other inner defect edges (Fig. 3 structure 1, 2, 3, and 4). Subsequently, the influence of introducing a second N atom is taken into account by considering various models with graphitic-graphitic, pyridinic-graphitic, pyrrolic-graphitic, and pyridinic-pyridinic N pairs. Pyrrolic-pyrrolic and pyrrolic-pyridinic N pairs are not taken into account since these pairs are separated by larger distances than the 2-3 bond distances

that are possible to probe via HMQC solid-state NMR.[41] The simulated 2D ^{13}C-^{15}N results are shown in Fig. 2. For each inequivalent C atom as a first neighbor of N atoms, a C-N data point is added using the simulated ^{13}C and ^{15}N chemical shift. Because both the number of equivalent C atoms, and the ratio of different modeling structures are not taken into account, the point density in a certain region cannot be quantitatively linked with the experimental signal intensity. The symbol type indicates the presence and distance (in the term of bonds) of other nearby N atoms. Circles stand for N atoms without other N atoms within three bond distances. Triangles represent N atoms with a nearby N as second neighbor and squares represent N atoms with a third neighbor N. The color indicates the type of the local N structure: blue represents graphitic N atoms, which are bonded to three C atoms. Orange represents pyridinic N atoms, which are bonded to 2 C atoms. White represents pyrrolic N atoms, which are bonded to 2 C atoms and 1 H atom. For triangles and squares, the left half indicates the type of the probed N atom and the right half indicates the type of neighbor N atom. The match between the calculated and experimental chemical shifts will be investigated in the next step.

In general, the calculated ^{13}C and ^{15}N isotropic chemical shifts match well with the experimental data (as shown in Fig. 2) and explain the observed signal broadening. A perfect match is not necessary, since some local structures probed in the calculations might not be present in large enough quantities in the experimental sample to provide a detectable signal. The spectrum can be separated into two general regions. The upper region containing both pyrrolic N and graphitic N shows ^{15}N and ^{13}C chemical shifts in the ranges of 120-200 ppm and 110-160 ppm, respectively. The lower region containing various pyridinic structures shows intensity spanning the ranges of 220-280 ppm and 120-160 ppm for ^{15}N and ^{13}C isotropic chemical shifts, respectively. Comparison with previous ^{13}C and ^{15}N NMR chemical shift assignments of the various N-moieties in carbonaceous materials and graphitic carbon nitrides shows agreement with our assignments.[49–53] ^{15}N chemical shifts exhibit clear trends with respect to local N environments: pyrrolic N atoms have the lowest ^{15}N isotropic

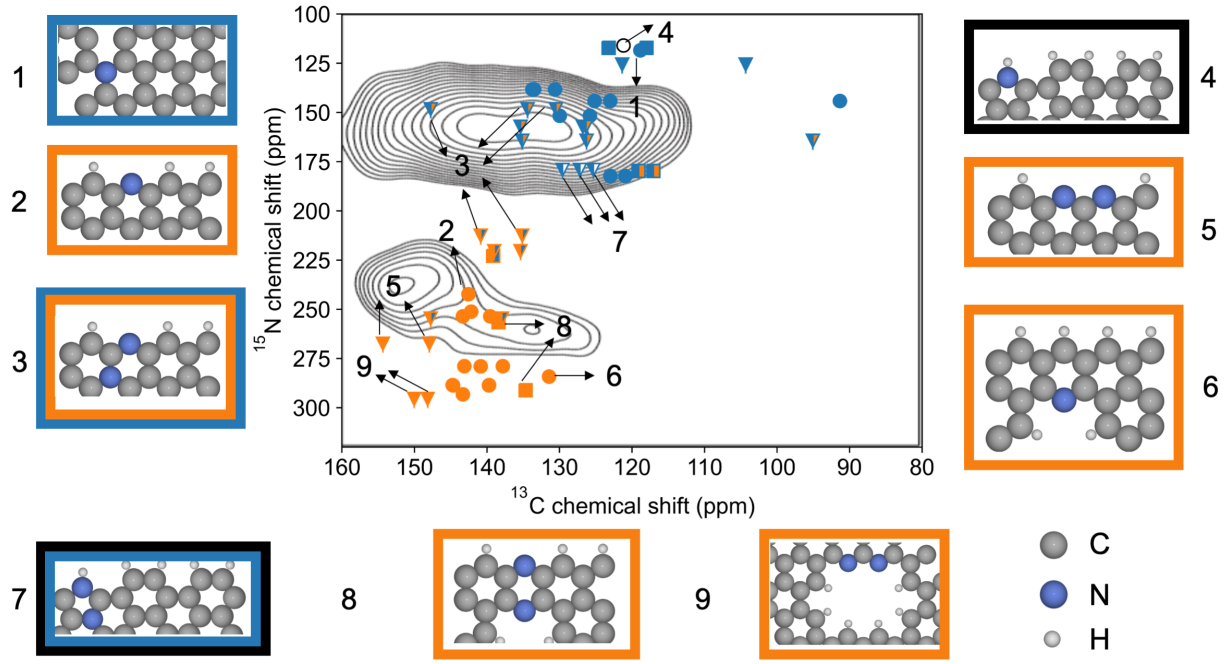

Figure 2: Simulated ^{13}C-^{15}N correlation NMR chemical shifts, together with the experimental 2D ^{13}C-^{15}N intensity. Experimentally, a mesoporous N-carbon material containing 16 atom% N was synthesized from a 1:3 molar ratio of cyclohexanehexone octahydrate and uniformly ^{13}C, ^{15}N-enriched urea, as described by Fechler et al.[37] Scatter points are simulated results and contour lines indicates experimental signal. The scatter styles indicate other nearby N atoms. Filled circles: atoms without other N atoms nearby, triangles:atoms with another N atom as second neighbor, squares: atoms with another N atom as third neighbor. The color indicates the type of the local N structure: blue for graphitic N atoms, orange for pyridinic N atoms and white for pyrrolic N atoms (with black outline when necessary). For triangles and squares, the left half indicates the type for the probed N atom and right half indicates the type for the neighbor N atom.

chemical shifts, followed by graphitic, and pyridinic N with the highest ^{15}N isotropic chemical shifts. This trend also holds for ^{13}C isotropic chemical shifts, although there are overlaps between different types of N environments. This can be understood by incorporating the the influence of the bonding environment: the pyrrolic and graphitic N atoms have 3 neighbors whereas pyridinic N has 2 neighbors, which leads to a decrease in the electron density on pyridinic N atoms and the adjacent C atoms. The relatively smaller difference between pyrrolic and graphitic N atoms stems from the electronegativity difference between C (2.55) and H (2.20): pyrrolic N and C atoms have a slightly larger electron density and hence

smaller chemical shift.

A more detailed understanding can be achieved by decomposing the structure-related broadening into two aspects: the geometric effect for the N atom itself, and the neighbor effect influenced by the proximity of other N atoms. The neighboring effect follows a general trend: a graphitic N neighbor decreases the ^{15}N isotropic chemical shifts of pyridinic N environments, and a pyridinic N neighbor increases the ^{15}N isotropic chemical shifts of graphitic and pyridinic N environments. This is consistent with the fact that the electron-rich graphitic N atom transfers some electronic density to its less rich pyridinic neighbor. Although graphitic N has a larger ^{15}N chemical shift than pyrrolic N (118.4 ppm >115.3 ppm), a graphitic N neighbor decreases the ^{15}N isotropic chemical shift of a pyrrolic N nuclei, and a pyrrolic N neighbor increases the ^{15}N isotropic chemical shift of a graphitic N nuclei. The influence of a graphitic N neighbor on an adjacent graphitic moiety is small: with a second or third graphitic N neighbor, the ^{15}N chemical shift changes from 118.4 ppm to 125.6 or 117.2 ppm, respectively. The influence of a pyridinic N neighbor on a pyridinic N center is complicated and no simple trend is found. The effect of pyridinic or pyrrolic N neighbors on a pyrrolic moiety are not investigated since they cannot act as close neighbors within a distance of three bonds. All the possible combinations of N moieties are explored and the calculated ^{15}N and ^{13}C chemical shifts explain a large part of the observed broadening of the spectrum in both dimensions.

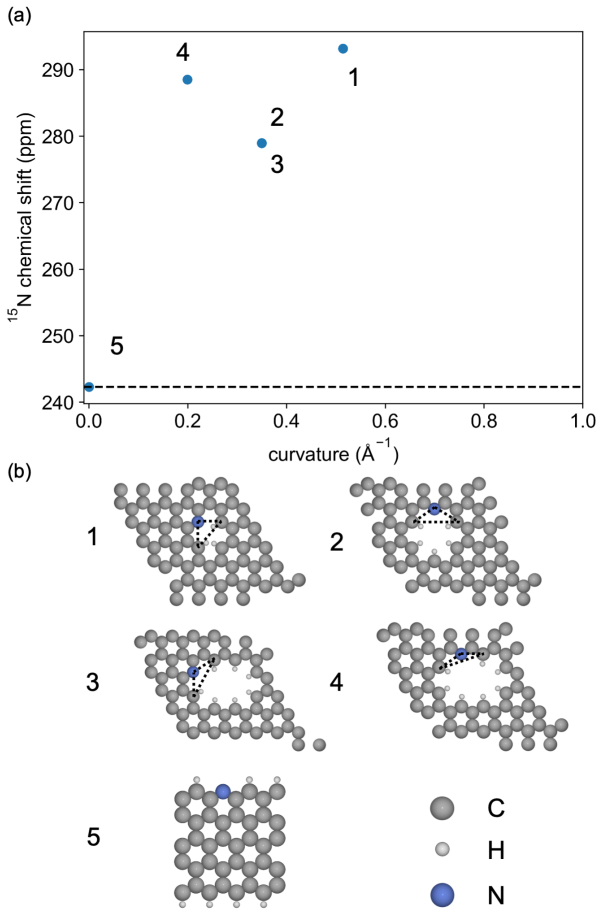

Figure 3: (a) Relationship between curvature and ^{15}N isotropic chemical shift. The dotted line indicates the ^{15}N isotropic chemical shift at the limit of zero curvature, i.e., simple edge pyridinic N at zigzag edge, structure 5 in (b). This is also structure 2 in Fig. 2. (b) Underlying structures of the data points appearing in (a). The models are listed in an order of decreasing curvature with atoms depicted as follows: grey: C, white: H, blue: N. Dotted lines indicate the N atom and the two most adjacent edge C atoms used to calculate the Menger curvature.

The influence of the morphology on the ^{13}C and ^{15}N isotropic chemical shifts of the graphene edges, straight or curved at vacancy islands can be quantified by the the Menger curvature c, which is the reciprocal of the radius of the circle that passes through three points.[54] This descriptor captures the local curvatures of the signaling C/N atoms. The center N atom and two most adjacent edge C atoms give 3 2D positions, x_1, x_2, and x_3. The

Menger curvature is defined by:

$$c(x_1, x_2, x_3) = \frac{4A}{\|x_1 - x_2\|\|x_2 - x_3\|\|x_3 - x_1\|} \tag{3}$$

where A denotes the area of the triangle spanned by x_1, x_2, and x_3. The symbol $\|\|$ denotes the L^2 norm in the 2D space.

Thus, the ^{15}N isotropic chemical shifts can be correlated with the curvatures, which are a descriptor of the local geometry. This relationship in different N-doped graphene systems is shown in Fig. 3. The idea of local curvature is validated via the data point of N-doped 6C defected terrace model: Fig. 3 (b), structure 2, and the data point of N-doped 10C defected terrace model: Fig. 3 (b), structure 3. Although globally these two structures are very different, the local curvatures of these two N atoms are rather similar and the ^{15}N chemical shifts are very close. The 6C and 10C defected terrace model are created by removing 6 and 10 C atoms from the pristine terrace model, saturating dangling bonds with H atoms and substituting one edge C-H pair with a N atom. The local geometry effect correlates the extent of defect curvature with ^{15}N chemical shifts. Specifically, environments with increased local curvature are found to have increasing chemical shifts (Fig. 3). This is similar to the relationship between surface curvature and ^{13}C chemical shifts in carbon nanotube systems.[25]

NMR detects differences in electronic shielding which is manifested as differences in isotropic chemical shifts and which can intuitively be connected to atomic charge.[55] In Fig. 4, the relationship between the DDEC6 charge of the signal atom and the curvatures is shown. The data points generally follow a trend: the smaller the charge, i.e., the higher the electron density, the more shielded the nucleus and hence the smaller the chemical shift. For N-doped systems, the larger the curvature, the more positive the charge, meaning the curvature hinders N atoms taking electrons from neighbor C atoms.

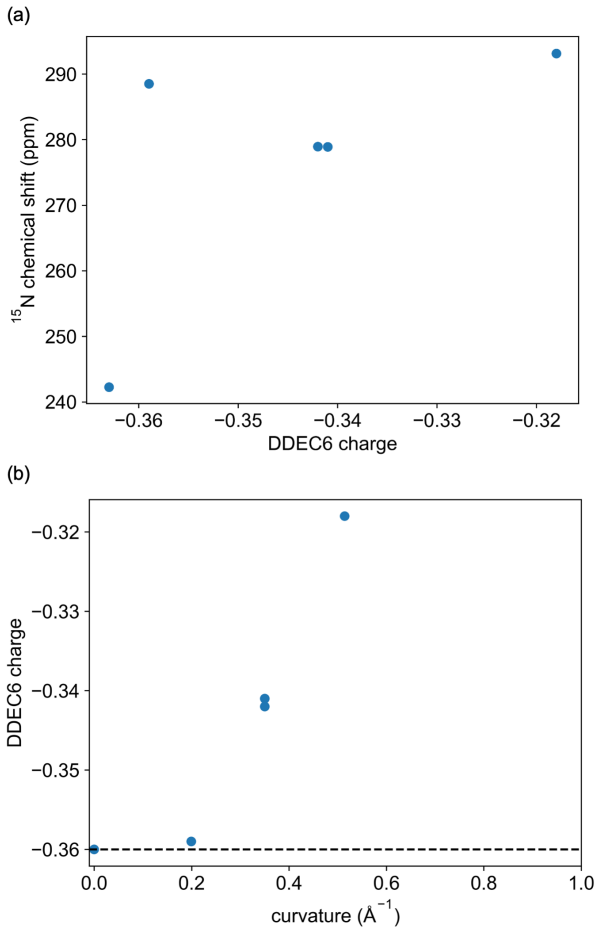

Figure 4: The relationship between (a) atomic charge and chemical shift and (b) charge and curvature of the models shown in Fig. 3 (b). Negative values denote an accumulation of electron density (negative charge), positive values indicate electron density depletion (positive charge).

Now that the atomic charge descriptor has been established, both the ^{15}N and ^{13}C chemical shifts of the 2D NMR spectrum (Fig. 2) can be analyzed and correlated using this descriptor. Fig. 5 shows the relationship between atomic charges and chemical shifts for N and C atoms, in panels (a) and (b), respectively. Once again, both ^{13}C and ^{15}N chemical shifts follow a general trend: within each type, more negative charge (higher electron density) corresponds to more shielding (thus, smaller chemical shifts).

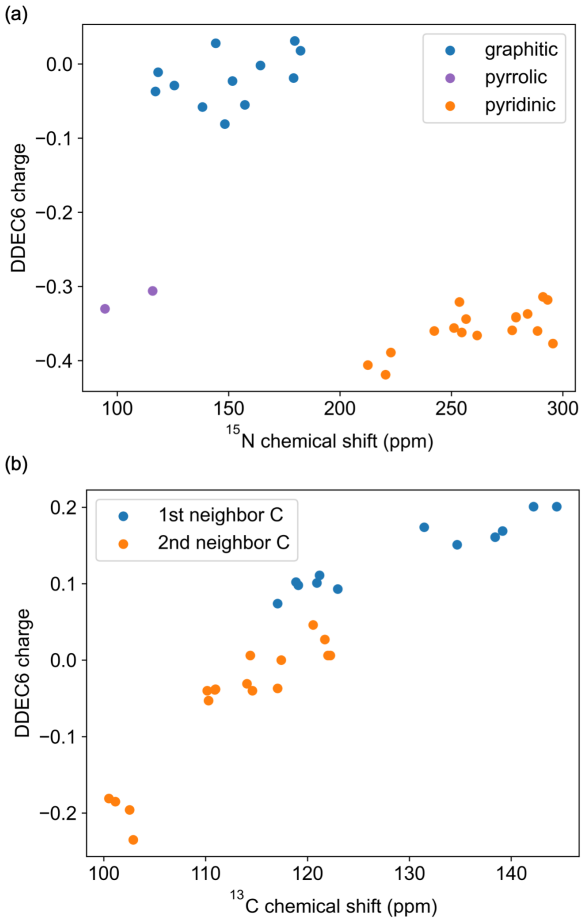

Figure 5: The relationship between charge and chemical shift of (a) N atoms and (b) C atoms as first and second neighbor of N atoms from the models utilized in this study. Negative values denote an accumulation of electron density (negative charge), positive values indicate electron density depletion (positive charge).

Interestingly, unlike the ^{13}C chemical shifts in Fig. 5(b) following a single scaling relation, different N species give different offsets. Differences in first neighbors of the center N atoms explain the differences in offsets: 2 C atoms for pyridinic N centers, 3 C atoms for graphitic N centers, and 2 C atoms with 1 H atom for pyrrolic N centers. It is also worth mentioning that the second C neighbors, although not shown in Fig. 2, show generally negative charge, whereas first neighbor C atoms show generally positive charge. As N has a greater electronegativity (3.04) than C (2.55), electron density is transferred from the first neighbor to N, creating a depletion zone around the N atom. The second neighbor C atom experiences increased electron density, forming a charge ripple. This also contributes to the broadening

of ^{13}C chemical shifts.

Experimentally, water is used to probe the presence of N species on the material surface. Thus, modeling this effect is crucial for understanding experimental results under such operating conditions. The interaction between surface adsorbed water and surface N atoms varies strongly with respect to the type of N atom, see SI Fig. S4 for structures. For a pyrrolic N atom, the O atom from water forms a hydrogen bond with the H atom from the pyrrolic NH group. Since O has a greater electronegativity (3.44) than N (3.04) and H (2.20), the electron density is transferred from NH to O. Thus, the N and H nuclei are both effectively deshielded and accordingly exhibit larger ^{15}N and ^{1}H isotropic chemical shifts, as shown in Fig. 6. To test the convergence of this effect with the number of water molecules, up to four water molecules are added to the pyrrolic N model, and the influence after three molecules added is small, see Fig. 6.

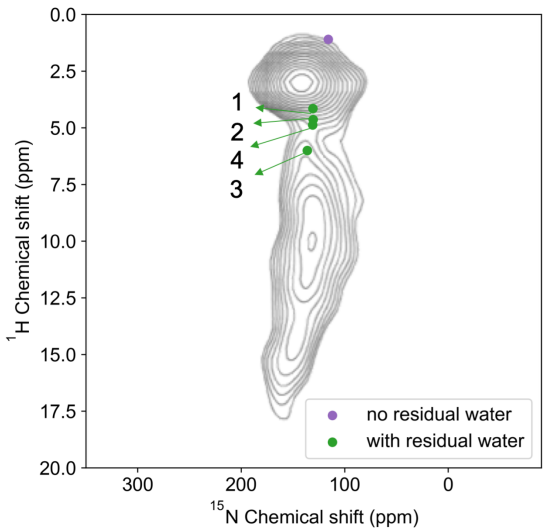

Figure 6: Simulated and experimental 2D ^{15}N-^{1}H NMR correlation for a 16 atom% N graphitic N-carbon material. Scatter points are simulated results and contour lines indicate experimental signal intensity. The data points shown are from pyrrolic N model with 0, 1, 2, 3, and 4 water molecules. Numbers next to scatters indicate the numbers of water molecules in the models.

Residual water has an effect on the other two types of N atoms, but this is not directly

reflected in the 2D spectrum of Fig. 6 since there's no first neighbor H of pyridinic N and graphitic N. For pyridinic N, interactions with adsorbed water results in greater shielding of the pyridinic ^{15}N nucleus and corresponding deshielding of the ^{1}H nucleus in water. It is also found that the O atom, instead of the H atom, will interact with the graphitic N atom. As a result, graphitic N is deshielded, but this is not reflected on the 2D ^{15}N-^{1}H spectrum since the distance from the water H atom to graphitic N atom is large. For the 2D ^{13}C-^{15}N spectra, the overall result of water coordination is that the ^{15}N chemical shift of pyrrolic N will be shifted towards larger values with a magnitude of 15-20 ppm, graphitic N will be shifted towards larger values with a magnitude of about 6 ppm and pyridinic N will be shifted towards smaller values with a magnitude of about 25 ppm. Detailed values are listed in SI table S5. If we consider the Gibbs free energy change of water on graphitic/pyrrolic/pyridinic moieties, as shown in SI table S6, we find that water adsorption is favorable on pyrrolic and pyridinic N sites. This explains why in Fig. 2, where water adsorption is not included, the pyrrolic structure (4) appears with an underestimated chemical shift compared to the experimental data, and why some pyridinic group chemical shifts are overestimated. Correction for the influence of water significantly improves the agreement. The influence of residual water on the ^{15}N and ^{1}H isotropic chemical shifts can also be reflected on the atomic charge, see SI Fig. S5. This influence is relevant for applications since it indicates that the electronic properties will be altered when the materials are in electrocatalytic conditions.

Conclusion

DFT calculations are used in this work to predict and explain the chemical shifts of N, C, H atoms in N-doped graphene systems. A number of different models are investigated: non-doped models (terrace, zigzag edge, and armchair edge), single N-doped models (graphitic, pyridinic, and pyrrolic N), and N pair models (graphitic-graphitic, pyridinic-pyridinic, pyrrolic-graphitic, and pyridinic-pyridinic). Comparisons of predicted chemical

shifts with experimental 2D ^{13}C-^{15}N spectra show good agreement, especially when the influence of water adsorption is included. The major difference between the chemical shifts of graphitic/pyridinic/pyrrolic N-moieties is understood by comparing the electronegativities of the various environments.

Furthermore, for each type of environment, the general concept of signal broadening is decomposed into four different factors, the influences of which are discussed in detail. The first factor is the standalone N/C geometry, where a larger curvature of the graphene edge is found to give a more positive chemical shift. The second factor is the effect of a second N atom nearby: a graphitic N atom close to a pyridinic N decreases the chemical shift, while a pyridinic N close to a graphitic N increases the chemical shift. The trends of other types of moiety mixing are more complicated, but the overall signal broadening matches the experimental spectrum well. The third factor is that for each specific structure, the second neighbor C atom experiences a lower chemical shift. The fourth factor is the influence of residual water, which is important to understand the aqueous environment in oxygen reduction reaction or hydrogen evolution reaction. Introduction of this factor matches with the experimental 2D ^{15}N-^{1}H spectrum and provides better agreement with the experimental ^{13}C-^{15}N spectrum. With the free energy taken into account, water adsorption on pyrrolic and pyridinic N sites is found to be more stable and to induce a positive or negative deviation in the chemical shift, respectively.

An intuitive correlation between the charge of the probed atom and the chemical shift is confirmed: the smaller the charge, i.e., the higher the electron density, the more shielded the nucleus is, and hence the smaller the chemical shift. The relationship between charge and chemical shifts is discussed, enabling a more detailed understanding of the electronic influence of N doping. These results can be used for the rational design of N-containing carbon materials with desirable electronic properties to improve electrochemical performance. They can also lead to a determination of the nature of active sites in these electrocatalysts by comparison of several N-doped carbon materials.

Acknowledgement

This work is supported by the Center for Synthetic Control Across Length-scales for Advancing Rechargeables, an Energy Frontier Research Center funded by the US Department of Energy, Office of Science Basic Energy Sciences programme under award DE-SC0019381. The calculations were performed on the Hoffman2 cluster at UCLA Institute for Digital Research and Education (IDRE) and the Extreme Science and Engineering Discovery Environment (XSEDE),[56] which is supported by National Science Foundation grant number ACI-1548562, through allocation TG-CHE170060.

Associated Content

supplementary information: supplementary Figs. 1-5, Tables 1-6, and discussions. structure.txt: atomic coordinates of models used in this work in VASP format

References

(1) Reddy, A. L. M.; Srivastava, A.; Gowda, S. R.; Gullapalli, H.; Dubey, M.; Ajayan, P. M. Synthesis Of Nitrogen-Doped Graphene Films For Lithium Battery Application. *ACS Nano* **2010**, *4*, 6337–6342.

(2) Xu, Y.; Lin, Z.; Zhong, X.; Huang, X.; Weiss, N. O.; Huang, Y.; Duan, X. Holey graphene frameworks for highly efficient capacitive energy storage. *Nat. Commun.* **2014**, *5*, 1–8.

(3) Gong, K.; Du, F.; Xia, Z.; Durstock, M.; Dai, L. Nitrogen-Doped Carbon Nanotube Arrays with High Electrocatalytic Activity for Oxygen Reduction. *Science* **2009**, *323*, 760–764.

(4) Zhao, Y.; Nakamura, R.; Kamiya, K.; Nakanishi, S.; Hashimoto, K. Nitrogen-doped

carbon nanomaterials as non-metal electrocatalysts for water oxidation. *Nat. Commun.* **2013**, *4*, 1–7.

(5) Lefèvre, M.; Proietti, E.; Jaouen, F.; Dodelet, J.-P. Iron-Based Catalysts with Improved Oxygen Reduction Activity in Polymer Electrolyte Fuel Cells. *Science* **2009**, *324*, 71–74.

(6) Wang, H.; Maiyalagan, T.; Wang, X. Review on Recent Progress in Nitrogen-Doped Graphene: Synthesis, Characterization, and Its Potential Applications. *ACS Catal.* **2012**, *2*, 781–794.

(7) Deng, D.; Pan, X.; Yu, L.; Cui, Y.; Jiang, Y.; Qi, J.; Li, W.-X.; Fu, Q.; Ma, X.; Xue, Q.; Sun, G.; et al, Toward N-Doped Graphene via Solvothermal Synthesis. *Chem. Mater.* **2011**, *23*, 1188–1193.

(8) Li, X.; Wang, H.; Robinson, J. T.; Sanchez, H.; Diankov, G.; Dai, H. Simultaneous Nitrogen Doping and Reduction of Graphene Oxide. *J. Am. Chem. Soc.* **2009**, *131*, 15939–15944.

(9) Zhao, L. et al. Visualizing Individual Nitrogen Dopants in Monolayer Graphene. *Science* **2011**, *333*, 999–1003.

(10) Baccile, N.; Laurent, G.; Coelho, C.; Babonneau, F.; Zhao, L.; Titirici, M.-M. Structural Insights on Nitrogen-Containing Hydrothermal Carbon Using Solid-State Magic Angle Spinning ^{13}C and ^{15}N Nuclear Magnetic Resonance. *J. Phys. Chem. C* **2011**, *115*, 8976–8982.

(11) Chmelka, B. F. Materializing opportunities for NMR of solids. *J. Magn. Reson.* **2019**, *306*, 91–97.

(12) Thomas, H. R.; Day, S. P.; Woodruff, W. E.; Vallés, C.; Young, R. J.; Kinloch, I. A.;

Morley, G. W.; Hanna, J. V.; Wilson, N. R.; Rourke, J. P. Deoxygenation of Graphene Oxide: Reduction or Cleaning? *Chem. Mater.* **2013**, *25*, 3580–3588.

(13) Mauri, F.; Louie, S. G. Magnetic Susceptibility of Insulators from First Principles. *Phys. Rev. Lett.* **1996**, *76*, 4246–4249.

(14) Pickard, C. J.; Mauri, F. All-electron magnetic response with pseudopotentials: Nmr chemical shifts. *Phys. Rev. B* **2001**, *63*, 245101.

(15) Yates, J. R.; Pickard, C. J.; Mauri, F. Calculation of NMR chemical shifts for extended systems using ultrasoft pseudopotentials. *Phys. Rev. B* **2007**, *76*, 024401.

(16) Profeta, M.; Mauri, F.; Pickard, C. J. Accurate First Principles Prediction of ^{17}O NMR Parameters in SiO_2: Assignment of the Zeolite Ferrierite Spectrum. *J. Am. Chem. Soc.* **2003**, *125*, 541–548.

(17) D'Anna, V.; Norsic, S.; Gajan, D.; Sanders, K.; Pell, A.; Lesage, A.; Monteil, V.; Copéret, C.; Pintacuda, G.; Sautet, P. Structural Characterization of the EtOH–$TiCl_4$–$MgCl_2$ Ziegler–Natta Precatalyst. *J. Phys. Chem. C* **2016**, *120*, 18075–18087.

(18) Kerber, R. N.; Kerber, T.; Rozanska, X.; Delbecq, F.; Sautet, P. Grafting trimethylaluminum and its halogen derivatives on silica: General trends for ^{27}Al SS-NMR response from first principles calculations. *Phys. Chem. Chem. Phys.* **2015**, *17*, 26937–26945.

(19) Stievano, L.; Tielens, F.; Lopes, I.; Folliet, N.; Gervais, C.; Costa, D.; Lambert, J.-F. Density Functional Theory Modeling and Calculation of NMR Parameters: An ab Initio Study of the Polymorphs of Bulk Glycine. *Cryst. Growth Des.* **2010**, *10*, 3657–3667.

(20) Thonhauser, T.; Ceresoli, D.; Marzari, N. NMR shifts for polycyclic aromatic hydrocarbons from first-principles. *Int. J. Quantum Chem.* **2009**, *109*, 3336–3342.

(21) Özcan, N.; Vähäkangas, J.; Lantto, P.; Vaara, J. Characteristic Spectral Patterns in

the Carbon-13 Nuclear Magnetic Resonance Spectra of Hexagonal and Crenellated Graphene Fragments. *ChemPhysChem* **2014**, *15*, 1799–1808.

(22) Vähäkangas, J.; Ikäläinen, S.; Lantto, P.; Vaara, J. Nuclear magnetic resonance predictions for graphenes: Concentric finite models and extrapolation to large systems. *Phys. Chem. Chem. Phys.* **2013**, *15*, 4634.

(23) Skachkov, D.; Krykunov, M.; Kadantsev, E.; Ziegler, T. The Calculation of NMR Chemical Shifts in Periodic Systems Based on Gauge Including Atomic Orbitals and Density Functional Theory. *J. Chem. Theory Comput.* **2010**, *6*, 1650–1659.

(24) de Souza, F. A.; Ambrozio, A. R.; Souza, E. S.; Cipriano, D. F.; Scopel, W. L.; Freitas, J. C. NMR Spectral Parameters in Graphene, Graphite, and Related Materials: Ab Initio Calculations and Experimental Results. *J. Phys. Chem. C* **2016**, *120*, 27707–27716.

(25) Casabianca, L. B. Effect of Curvature on Carbon Chemical Shielding in Extended Carbon Systems. *J. Phys. Chem. A* **2016**, *120*, 7011–7019.

(26) Zhang, Y.; Hao, J.; Li, J.; Hao, C. Theoretical study of triiodide reduction reaction on nitrogen-doped graphene for dye-sensitized solar cells. *Theor. Chem. Acc.* **2016**, *135*, 23.

(27) Kresse, G.; Hafner, J. Ab initio molecular dynamics for liquid metals. *Phys. Rev. B* **1993**, *47*, 558.

(28) Perdew, J. P.; Burke, K.; Ernzerhof, M. Generalized Gradient Approximation Made Simple. *Phys. Rev. Lett.* **1996**, *77*, 3865–3868.

(29) Steinmann, S. N.; Corminboeuf, C. A generalized-gradient approximation exchange hole model for dispersion coefficients. *J. Chem. Phys.* **2011**, *134*, 044117.

(30) Steinmann, S. N.; Corminboeuf, C. Comprehensive Benchmarking of a Density-Dependent Dispersion Correction. *J. Chem. Theory Comput.* **2011**, *7*, 3567–3577.

(31) Mason, J. Conventions for the reporting of nuclear magnetic shielding (or shift) tensors suggested by participants in the NATO ARW on NMR shielding constants at the University of Maryland, College Park, July 1992. *Solid State Nucl. Mag.* **1993**, *2*, 285–288.

(32) Bertani, P.; Raya, J.; Bechinger, B. ^{15}N chemical shift referencing in solid state NMR. *Solid State Nucl. Mag.* **2014**, *61-62*, 15–18.

(33) Manz, T. A.; Limas, N. G. Introducing DDEC6 atomic population analysis: Part 1. Charge partitioning theory and methodology. *RSC Adv.* **2016**, *6*, 47771–47801.

(34) Limas, N. G.; Manz, T. A. Introducing DDEC6 atomic population analysis: Part 2. Computed results for a wide range of periodic and nonperiodic materials. *RSC Adv.* **2016**, *6*, 45727–45747.

(35) Separovic, F.; Naito, A. *Advances in Biological Solid-State NMR: Proteins and Membrane-Active Peptides*; Royal Society of Chemistry, 2014.

(36) Levitt, M. H. *Spin dynamics: basics of nuclear magnetic resonance*; John Wiley & Sons, 2013.

(37) Fechler, N.; Zussblatt, N. P.; Rothe, R.; Schlögl, R.; Willinger, M.-G.; Chmelka, B. F.; Antonietti, M. Eutectic Syntheses of Graphitic Carbon with High Pyrazinic Nitrogen Content. *Adv. Mater.* **2015**, *28*, 1287–1294.

(38) Thurber, K. R.; Tycko, R. Measurement of sample temperatures under magic-angle spinning from the chemical shift and spin-lattice relaxation rate of ^{79}Br in KBr powder. *J. Magn. Reson.* **2009**, *196*, 84–87.

(39) Yesinowski, J. P.; Ladouceur, H. D.; Purdy, A. P.; Miller, J. B. Electrical and ionic

conductivity effects on magic-angle spinning nuclear magnetic resonance parameters of CuI. *J. Chem. Phys.* **2010**, *133*, 234509.

(40) Hu, B.; Trébosc, J.; Amoureux, J.-P. Comparison of several hetero-nuclear dipolar recoupling NMR methods to be used in MAS HMQC/HSQC. *J. Magn. Reson.* **2008**, *192*, 112–122.

(41) Kobayashi, T.; Singappuli-Arachchige, D.; Wang, Z.; Slowing, I. I.; Pruski, M. Spatial distribution of organic functional groups supported on mesoporous silica nanoparticles: A study by conventional and DNP-enhanced ^{29}Si solid-state NMR. *Phys. Chem. Chem. Phys.* **2017**, *19*, 1781–1789.

(42) Lesage, A.; Sakellariou, D.; Steuernagel, S.; Emsley, L. Carbon−Proton Chemical Shift Correlation in Solid-State NMR by Through-Bond Multiple-Quantum Spectroscopy. *J. Am. Chem. Soc.* **1998**, *120*, 13194–13201.

(43) Si, Y.; Samulski, E. T. Synthesis of Water Soluble Graphene. *Nano Lett.* **2008**, *8*, 1679–1682.

(44) Gao, W.; Alemany, L. B.; Ci, L.; Ajayan, P. M. New insights into the structure and reduction of graphite oxide. *Nat. Chem.* **2009**, *1*, 403–408.

(45) Marcano, D. C.; Kosynkin, D. V.; Berlin, J. M.; Sinitskii, A.; Sun, Z.; Slesarev, A.; Alemany, L. B.; Lu, W.; Tour, J. M. Improved Synthesis of Graphene Oxide. *ACS Nano* **2010**, *4*, 4806–4814.

(46) Stankovich, S.; Dikin, D. A.; Piner, R. D.; Kohlhaas, K. A.; Kleinhammes, A.; Jia, Y.; Wu, Y.; Nguyen, S. T.; Ruoff, R. S. Synthesis of graphene-based nanosheets via chemical reduction of exfoliated graphite oxide. *Carbon* **2007**, *45*, 1558–1565.

(47) Resing, H.; Weber, D.; Anderson, M.; Miller, G.; Moran, M.; Poranski Jr, C.; Mattix, L. NMR Shift Tensors for Polyacetylene and Graphite. *Polym. Prepr.* **1982**, *23*, 101.

(48) Darmstadt, H.; Roy, C.; Kaliaguine, S.; Xu, G.; Auger, M.; Tuel, A.; Ramaswamy, V. Solid state ^{13}C-NMR spectroscopy and XRD studies of commercial and pyrolytic carbon blacks. *Carbon* **2000**, *38*, 1279–1287.

(49) Kuroki, S.; Nabae, Y.; Chokai, M.; Kakimoto, M.-a.; Miyata, S. Oxygen reduction activity of pyrolyzed polypyrroles studied by ^{15}N solid-state NMR and XPS with principal component analysis. *Carbon* **2012**, *50*, 153–162.

(50) Gammon, W.; Hoatson, G.; Holloway, B.; Vold, R.; Reilly, A. Bonding in hard and elastic amorphous carbon nitride films investigated using ^{15}N, ^{13}C, and ^{1}H NMR spectroscopy. *Phys. Rev. B* **2003**, *68*, 195401.

(51) Huo, J.; Duan, P.; Pham, H. N.; Chan, Y. J.; Datye, A. K.; Schmidt-Rohr, K.; Shanks, B. H. Improved hydrothermal stability of Pd nanoparticles on nitrogen-doped carbon supports. *Catal. Sci. Technol.* **2018**, *8*, 3548–3561.

(52) Hu, Y.; Shim, Y.; Oh, J.; Park, S.; Park, S.; Ishii, Y. Synthesis of ^{13}C-,^{15}N-Labeled Graphitic Carbon Nitrides and NMR-Based Evidence of Hydrogen-Bonding Assisted Two-Dimensional Assembly. *Chem. Mater.* **2017**, *29*, 5080–5089.

(53) Wang, X.; Hou, Z.; Ikeda, T.; Terakura, K. NMR Chemical Shifts of ^{15}N-Bearing Graphene. *J. Phys. Chem. C* **2014**, *118*, 13929–13935.

(54) Leger, J. Menger Curvature and Rectifiability. *Ann. Math.* **1999**, *149*, 831.

(55) Farnum, D. *Advances in Physical Organic Chemistry Volume 11*; Elsevier, 1975; Vol. 11; pp 123–175.

(56) Towns, J.; Cockerill, T.; Dahan, M.; Foster, I.; Gaither, K.; Grimshaw, A.; Hazlewood, V.; Lathrop, S.; Lifka, D.; Peterson, G. D.; Roskies, R.; Scott, J. R.; Wilkins-Diehr, N. XSEDE: Accelerating Scientific Discovery. *Comput. Sci. Eng.* **2014**, *16*, 62–74.

Graphical TOC Entry